







Original Article


Effects of sand sedimentation and wind erosion around sand barrier: Numerical simulation and wind tunnel test studies


ZHANG Kai^{1,2*}  <https://orcid.org/0000-0002-4760-8860>;  e-mail: zhangkai0212@yeah.net

ZHANG Hai-long¹  <https://orcid.org/0000-0003-2499-505X>; e-mail: 18419692148@163.com

DENG Yu-hui^{1*}  <https://orcid.org/0000-0003-4796-2875>;  e-mail: 13893225694@163.com

QU Jian-jun²  <https://orcid.org/0000-0002-1141-9873>; e-mail: 827539471@qq.com

WANG Zheng-hui¹  <https://orcid.org/0000-0002-0642-8038>; e-mail: 1472264092@qq.com

LI Sheng¹  <https://orcid.org/0000-0003-0118-3876>; e-mail: 827050577@qq.com

*Corresponding author

¹ College of Civil Engineering, Lanzhou Jiaotong University, Lanzhou 730000, China

² Key Laboratory of Desert and Desertification, Northwest Institute of Eco-Environment and Resources, Chinese Academy of Sciences, Lanzhou 730000, China

Citation: Zhang K, Zhang HL, Deng YH, et al. (2023) Effects of sand sedimentation and wind erosion around sand barrier: Numerical simulation and wind tunnel test studies. *Journal of Mountain Science* 20(4). <https://doi.org/10.1007/s11629-022-7757-z>

© Science Press, Institute of Mountain Hazards and Environment, CAS and Springer-Verlag GmbH Germany, part of Springer Nature 2023

Abstract: Based on numerical simulations, this study highlights the sedimentation and erosion problems around a sand barrier through the relationship between the shear stress of the surface around the sand barrier and the critical shear stress of sand grains. The numerical simulation results were verified using data measured by the wind tunnel test. The results showed that when the porosity was the same, the size and position of the vortex on the leeward side of the sand barrier were related to the inlet wind speed. As the wind speed increased, the vortex volume increased and the positions of the separation and reattachment points moved toward the leeward side. When the porosity of the sand barrier was 30%, the strength of the acceleration zone above the sand barrier was the highest, and the strength of the acceleration zone was negatively correlated with the porosity. Sand erosion and sedimentation distance were related to wind speed. With an increase in wind speed, the sand grain

forward erosion or reverse erosion areas on the leeward side of the sand barrier gradually replaced the sedimentation area. With an increase in porosity, the sand sedimentation distance on the leeward side of the sand barrier gradually shortened, and the sand erosion area gradually disappeared. The sand sedimentation distance on the leeward side of the sand barrier with 30% porosity was the longest. The numerical simulation results were in good agreement with the wind tunnel test results. Based on the sand erosion and sedimentation results of the numerical simulation and wind tunnel test, when the porosity was 30%, the protection effect of the High Density Polyethylene (HDPE) board sand barrier was best.

Keywords: Sand sedimentation; Wind erosion; Numerical simulation; Wind tunnel test

1 Introduction

Traffic road construction is an important part of

Received: 08-Oct-2022

Revised: 07-Dec-2022

Accepted: 11-Jan-2023

social development, and it is closely related to people's production and life. It can be considered as a structure and it can be affected by various natural factors. Among these, the impact of sandstorm activities on structures has attracted increasing attention. In desert areas, local shear stress occurs on the ground under the action of the wind. When the local shear stress on the ground is greater than the critical shear stress of the sand grains, the sand grains move away from the surface and move with the wind, forming a wind-sand flow (Wang et al. 2018). In recent years, railways in sandy areas in China have developed rapidly and sandstorm disasters have had a serious impact on most railway transportation in the area. The impact of wind-sand flow on railway operation mainly includes the following two aspects: (1) Erosion of embankments: both sides of the embankment are eroded by wind-sand flow, which affects the reliability of the embankment over time (Bruno et al. 2018). (2) Sand accumulation on the embankment: Owing to the obstruction of the embankment, sand particles accumulate on the embankment or even bury the track bed, causing serious safety hazards (Zhang et al. 2022). Wind erosion and sand burial cause serious damage to traffic facilities, posing a significant threat to driving safety.

Scholars around the world have researched three types of sand control measures in the engineering practice of sand control for decades (Dong et al. 2007; Wang et al. 2017). The three types are mechanical, chemical, and plant measures. Among them, plant measures are one of the most fundamental and effective methods to control sand damage, but the environment along railway lines in most sandy areas is harsh and precipitation is scarce, so plant measures are difficult to apply practically. Chemical measures during the construction process are complicated and expensive. Mechanical measures have the advantages of convenient construction, low technical requirements, rapid results, and significant protection benefits. Therefore, mechanical measures are widely used to protect against railway sandstorms (Zhang et al. 2021).

In recent years, domestic and foreign scholars have conducted extensive research on the protective benefits of high vertical sand barriers. Hagen et al. (2012) found that the leeward side of a shelter belt with a porosity of 40% produced minimum wind speed during field observations. Perera (1981)

measured the velocity distribution on the leeward side of a sand barrier using an anemometer through wind tunnel tests. They found that when the porosity of the sand barrier was approximately 30%, the Reynolds shear force and turbulent kinetic energy on the leeward side of the sand barrier were the strongest. Lee and Kim (1999) measured the airflow velocity field and pressure distribution characteristics and found that sand barriers with porosities between 30% and 40% could effectively reduce the average velocity and surface pressure fluctuations on the leeward side of the sand barrier. Moreover, with the increase in porosity, the turbulence performance on the leeward side of the sand barrier and the average wind speed decreased (Wang et al. 2017; Wang et al. 2018). These high vertical sand barriers are mainly made of materials such as polythene (PE) nets, wheat grass, and reeds, which have a limited protection life (Zhang et al. 2020), and their durability is tested severely in plateau low-pressure areas.

In recent years, researchers have developed a new type of High Density Polyethylene (HDPE) board high vertical sand barrier, which is suitable for harsh environments, such as alpine regions, and areas with high salinity, and high wind energy. Some scholars have studied the sand control performance of sand barriers. Li et al. (2019) studied the sand control mechanism and effect of an HDPE board sand barrier with a porosity of 46% through wind tunnel tests and field test data. Qu et al. (2014) compared and analyzed the wind protection benefits of HDPE board functional sand-fixing barriers through wind tunnel tests. The average porosity of the three types of sand control nets used was approximately 30%, which is the optimal porosity of the sand control nets. Zhang et al. (2019, 2020) verified through numerical simulations and wind tunnel tests that when the porosity was 30%, the wind speed on the leeward side of a high vertical sand barrier of the HDPE board was the smallest, and the recovery range was the farthest from the sand barrier. The above studies compared the protection benefits of sand barriers with different porosities through wind tunnel tests and field observations. The results showed that the optimal porosity of the HDPE sand barriers was in the range of 30% to 50%. Unfortunately, these studies mainly evaluated the protection benefits of HDPE board sand barriers through changes in the wind-sand flow velocity, pressure distribution characteristics, and turbulent kinetic energy. Additionally, they did not

systematically study the sedimentation and erosion behavior of sand particles around the sand barriers.

Therefore, this study highlights the sedimentation and erosion problems around the sand barrier through the relationship between the surface shear stress around the sand barrier and the critical shear stress of the sand grains. At the same time, the results of numerical simulation and wind tunnel test were compared and analyzed, including the wind-sand flow field, wind-speed profile, sedimentation, and erosion characteristics. This study clarified the flow field and sand sedimentation mechanism around HDPE board sand barrier, and has a positive guiding significance for the selection of sand barrier.

2 Computational Models

2.1 Numerical simulation

2.1.1 Mathematical model

In this study, a three-dimensional steady-state Reynolds-averaged Navier–Stokes (RANS) model was used for the simulation, and the entire governing equation was expressed in Cartesian coordinates as

$$\frac{\partial \bar{V}_i}{\partial X_i} = 0 \tag{1}$$

$$\bar{V}_j \frac{\partial \bar{V}_i}{\partial X_j} = -\frac{1}{\rho} \frac{\partial \bar{P}}{\partial X_i} + \frac{\partial}{\partial X_j} \left(\mu + \mu_t \frac{\partial \bar{V}_i}{\partial X_j} + \frac{\partial \bar{V}_j}{\partial X_i} \right) \tag{2}$$

$$\bar{V}_j \frac{\partial K}{\partial X_j} = \frac{\partial}{\partial X_j} \left[(\sigma_k \mu_t + \mu) \frac{\partial K}{\partial X_j} \right] + \bar{P}_k - \beta^* K \omega \tag{3}$$

$$\begin{aligned} \bar{V}_j \frac{\partial \omega}{\partial X_j} = & \frac{\partial}{\partial X_j} \left[(\sigma_\omega \mu_t + \mu) \frac{\partial \omega}{\partial X_j} \right] + C_{\omega 1} \frac{\omega}{K} P_k \\ & - C_{\omega 2} \omega^2 + (1 - F_1) \frac{2\sigma_{\omega 2}}{\omega} \frac{\partial K}{\partial X_i} \frac{\partial \omega}{\partial X_i} \end{aligned} \tag{4}$$

where \bar{V}_i and \bar{V}_j are the mean velocity in the i and j direction; X_i and X_j are the i and j direction along the x axis; P is the mean pressure; ρ is the air density; μ is the air kinematic viscosity; K is the turbulent kinetic energy; ω is the specific dissipation rate; $\mu_t = K/\omega$ is the turbulent kinematic viscosity; and the kinetic energy generation term \bar{P}_k is modeled by introducing a limiter to prevent turbulent kinetic energy in the stagnant region from creating turbulent flow:

$$\bar{P}_k = \min(P_k, 10\beta^* K \omega), P_k \approx \mu_t \frac{\partial \bar{V}_i}{\partial X_j} + \frac{\partial \bar{V}_j}{\partial X_i} \frac{\partial \bar{V}_i}{\partial X_j} \tag{5}$$

Definitions of the mixing function F_1 and the model main constants β^* , σ_k , σ_ω , $C_{\omega 1}$ and $C_{\omega 2}$ can be

found in Menter et al. (2003). In the simulation of the time-averaged flow field characteristics of the long-term morphological movement of sand dunes, the time scale of the turbulent flow characteristics was much smaller than the time scale of sand particle transportation. Therefore, unsteady flow can be ignored, and this means that the RANS method is suitable for simulating the flow field characteristics of the two-phase flow of wind and sand. Shear Stress Transfer (SST)^{k- ω} was chosen for the turbulence model because it has been shown to be accurate for bluff body aerodynamics. The SST^{k- ω} model is combined with the sand roughness wall function near the wall. The equivalent sand roughness height is $K_s = 9.793 Z_0 / C_s$, where $C_s = 0.5$ is the roughness constant, and Z_0 is the aerodynamic roughness length.

The three-dimensional (3D) model used is shown in Fig. 1. The origin of the coordinates was set at the entrance of the lower wall. The porosities of the 3D model of the sand barrier were 30%, 40%, and 50%. The height of the sand barrier was set to 1.5 m and the thickness was set to 2 cm. The distance between the inlet of the wind-sand flow and the windward side of the sand barrier was 40H (H is the height of the sand barrier), the distance between the leeward side of the sand barrier and the outflow was 60H, and the length of the sand barrier was 10H, which is the same as the width of the computational domain. The height of the computational domain was 20H. The computational domain used was set to a size larger than or equal to the computational size in previous similar studies (Zhang et al. 2019, Noguchi et al. 2019), in order to eliminate the influence of boundary conditions on the computational results.

The boundary conditions are illustrated in Fig. 1. We applied no-slip boundary conditions to the bottom wall and symmetric boundary conditions to the sides.

The velocity profile at the inlet is $V_0(Z) = \frac{v^*}{k} \ln\left(\frac{Z}{z_0}\right)$,

where v^* is the friction velocity, von Karman coefficient was $k = 0.41$, and Z_0 is the aerodynamic roughness length. This combination of velocity and turbulence was in equilibrium to ensure that the specified profile did not fall within the domain of further development.

2.1.2 Numerical methods

To ensure the quality of the grid, a hexagonal unstructured mesh was used to complete the division.

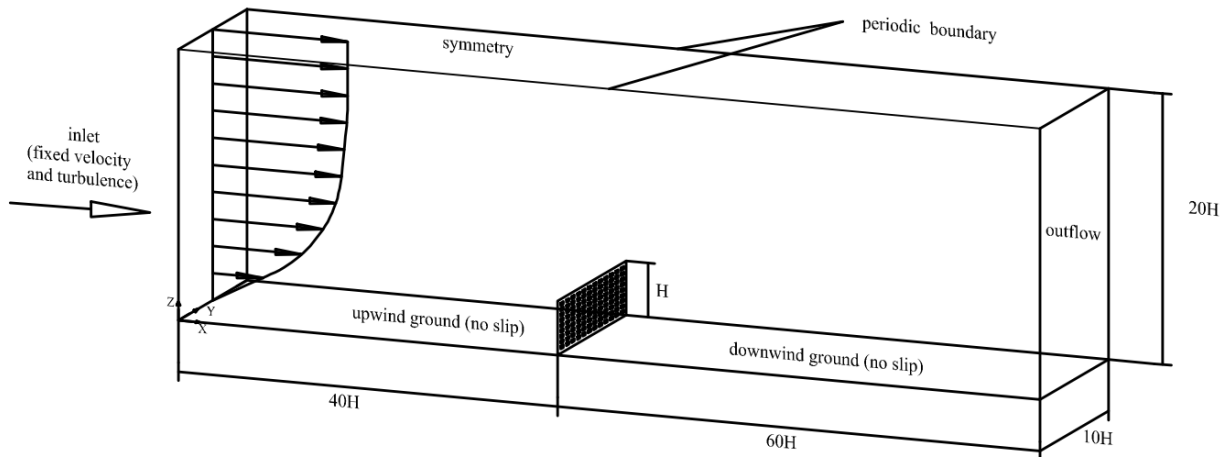


Fig. 1 The 3D computational domain and boundary conditions used in the simulation, all dimensions are expressed with reference to the HDPE board sand barrier height H (not drawn to scale for clarity).

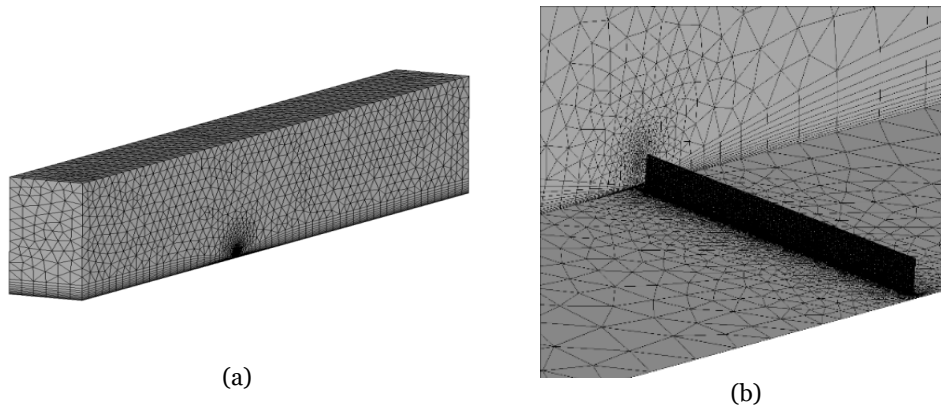


Fig. 2 (a) The hexahedral grid used for the whole area; (b) the meshing around the sand barrier in the local area.

The entire spatial watershed grid is shown in Fig. 2(a) and the grid near the sand barrier is shown in Fig. 2(b). When dividing the grid, the surrounding area of the sand barrier was accurately divided to ensure accurate simulation of the wind-sand flow around the sand barrier. The height of the boundary layer n_w provides a sufficient vertical mesh resolution to adequately resolve the flow variable gradient problem. n_w meets the requirements of the wall surface, that is, $30 < n^+ = n_p u^* / \nu < 200$, $n_w = 2n_p$, and n_p is the height of the grid center to meet the above standards, $100 \leq n^+ \leq 200$. The number of grids depended on the sand barrier used and the overall size. The total number of grids was 2.36×10^6 .

A steady-state solver was used for the Fluent simulation. The calculation settings included the finite volume method for the discrete control

equations, a momentum being adopted for the second-order upwind discrete scheme, and turbulent kinetic energy and turbulent dissipation rate being calculated using the second-order upwind formula (Lima et al. 2020). The SIMPLE algorithm was used for the pressure-velocity coupling. The convergence criterion of the scaled residual error was set to 10^{-6} for all the variables and the continuity equation, and the calculation was aggregated, except for the continuity equation (when the remaining ratio of the continuity equation reaches 10^{-4}). Additional iterations were performed until the residual ratio of all of the variables and the continuity equation were not further reduced (Yang et al. 2009). The source code Fluent was used.

The four incoming wind speeds used in this simulation were 8, 12, 16, and 20 m/s at an altitude of 15 m and the corresponding friction speeds at the entrance were 0.46, 0.56, 0.65, and 0.75 m/s,

respectively. These values exceeded the critical shear velocity of erosion corresponding to the sand particle diameter range of $d \in [0.063, 1.2]$ mm (Raffaele et al. 2016). Surface aerodynamic roughness length $z_0 = 0.003$ m.

Studies have shown that wind-induced sand shear force is closely related to sand erosion and sedimentation (Raffaele et al. 2016). The dimensionless ratios τ^* , $\tau^* = \frac{\tau_x}{|\tau_x|} \frac{|\tau|}{\tau_i}$, τ are the local shear stress on the ground, τ_x is the local shear stress in the X direction, τ_i is the critical shear stress of sand grains (Horvat et al. 2021), and the sand grain diameter $d=0.1$ mm is used for simulation (Tominaga et al. 2018, Zhang et al. 2022), the critical value of erosion shear stress for sand with this particle size is $\tau_i = 0.045$ Pa (Raffaele et al. 2016). Horvat et al. (2021) proposed the relationship between τ^* and sand erosion or sand deposition. The key factor is $\tau^* = \pm 1$ (erosion threshold) when $\tau^* > 1$ is forward erosion, when $-1 < \tau^* < 1$ is sedimentation, and when $\tau^* < -1$ is reverse erosion (Horvat et al. 2021). The point corresponding to the transition between sedimentation and erosion is called the sedimentation point. This paper uses this method to study the sand erosion and deposition around the sand barrier.

2.2 Wind tunnel test

2.2.1 Experimental Design

The wind tunnel test was conducted at the Wind Tunnel Laboratory of the Institute of Environment and Engineering in the Cold and Arid Regions of the Chinese Academy of Sciences. The total length of the wind tunnel is 37.78 m, the length of the working section is 16.23 m, the cross-sectional area is 0.6 m high and 1.0 m wide (inner wall size). The thickness of the boundary layer is up to 20 cm, and the wind speed in the wind tunnel can be adjusted in the range of 2-40 m/s (Dong et al. 2007).

The wind tunnel test was consisted of two parts: a flow field test and a sediment load test. The test inlet wind speeds at a height of 30 cm were 8, 12, 16, and 20 m/s, and HDPE plate models with 30%, 40%, and 50% porosity were tested (as shown in Fig. 3). The length, thickness, and height of the test model were

1.0 m, 2.0 mm, 15.0 cm, respectively.

The inlet wind speed was measured using a pitot-tube probe placed 30 cm above the ground. For the wind-speed profile measurements near the HDPE board sand barrier in the flow field test we made measurements on both the windward and leeward sides (on the windward side of the sand barrier 0.5H1 (P1), on the leeward side 0.25H1 (P2), 0.75H1 (P3), 2.5H1 (P4), 5H1 (P5), 7.5H1 (P6), and 12.5H1 (P7). It should be noted that H₁ was the height of the sand barrier model in the test. The gradient wind speed in the wind tunnel was measured using a pitot tube at heights of 0.4, 0.8, 1.2, 2.0, 4.0, 8.0, 12.0, 16.0, 20.0 and 24.0 cm. After each run, the pitot tube was moved to the next position for measurement. During the test, the wind-speed collection time was 20 s and the collection frequency was 0.5 s.

The sand bed in the sediment transport test was 4 m long and 5 cm thick, and the particle size was mainly 0.08 to 0.315 mm (average 0.118 mm). Before the test, a sand accumulation instrument was placed under the condition of no sand barrier, and the test duration under each wind speed was determined according to the capacity of the sand accumulation instrument. The durations were 4 min at 8 m/s, 3 min at 12 m/s, 2 min at 16 m/s, and 1.5 min at 20 m/s. The sand accumulation test was used to measure the length of sand accumulation on the windward and leeward sides of the sand barrier using a steel ruler after each test.

2.2.2 Wind tunnel similarity

In terms of geometric similarity, consideration of the ratio of the wind tunnel turbulent boundary layer to the ground-attached boundary layer is essential. Generally, the blocking degree does not exceed 6% in order to satisfy the requirements of avoiding wall interference. In this experiment, the ratio of the model to the actual field was 1:10, which satisfied geometric similarity. The height of the model produced in this experiment was 15 cm, and the thickness of the boundary layer of the wind tunnel could reach approximately 20 cm (Zhang et al. 2021), meaning that the model was in the boundary layer.

Motion similarity mainly considers the similarity of the flow state and wind-speed profile. The wind-speed profile was experimentally verified and conformed to the logarithmic motion law (Fig. 4). If the Reynolds number in the wind tunnel is sufficiently large, a self-simulation region independent of the

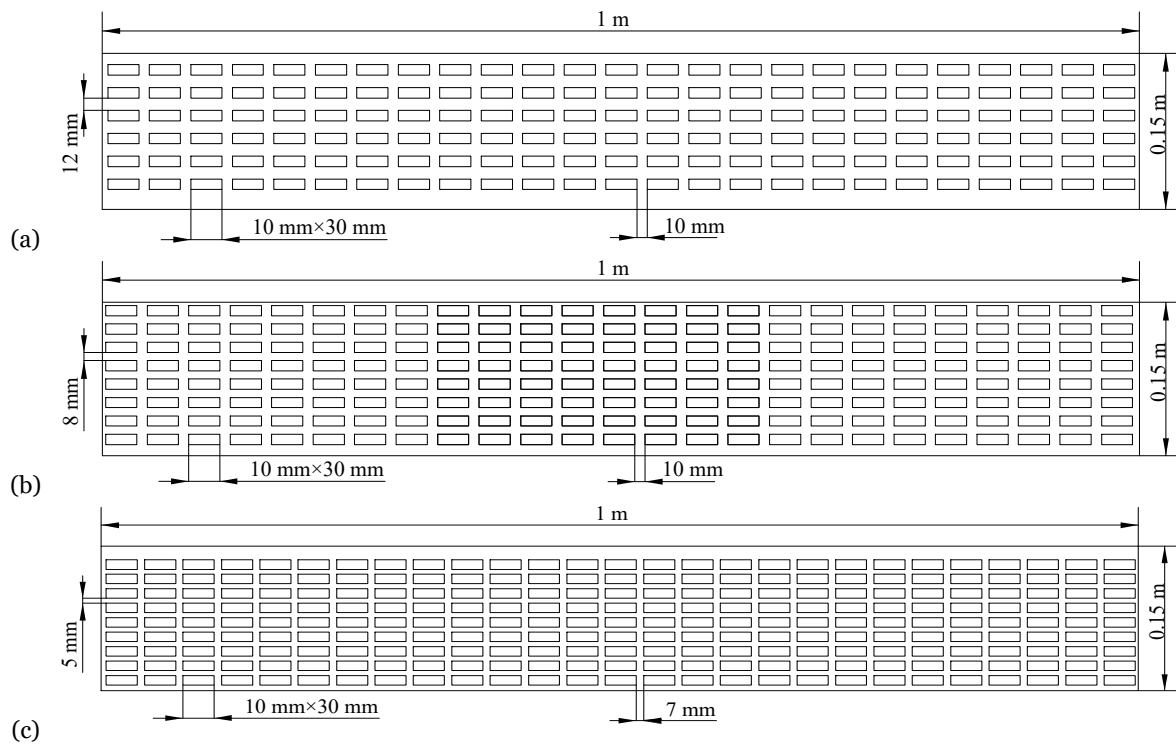


Fig. 3 Sand barriers of three HDPE boards with different porosities. (a) 30% porosity; (b) 40% porosity; (c) 50% porosity.

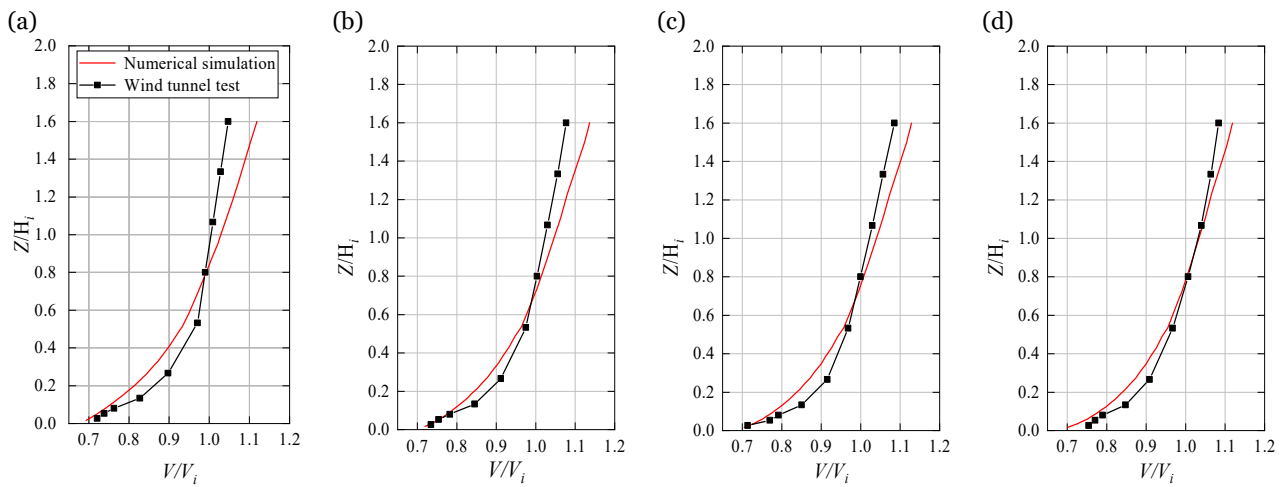


Fig. 4 Comparison of the dimensionless wind-speed profiles between the wind tunnel tests and numerical simulations under cavity conditions. (a)-(d) are the comparison of wind-speed profiles under the conditions of inlet wind speeds of 8, 12, 16 and 20 m/s, respectively. H_i represents the sand barrier heights H and H_1 in the numerical simulation and wind tunnel test, respectively, and V_i represents the velocity V and V_1 at the height of the sand barrier in the numerical simulation and wind tunnel test, respectively.

Reynolds number can be formed (White 1996). Four inlet wind speeds (8, 12, 16, and 20 m/s) were selected for the wind tunnel test. The Reynolds number ($Re = \rho vL / \mu$, where Re is the flow Reynolds number, represents the air density, $1.205 \text{ kg}\cdot\text{m}^{-3}$, v is the free-flow wind speed, L is the characteristic length, where this is the height of the sand barrier,

0.15 m , and μ is the air kinematic viscosity, $1.4 \times 10^{-5} \text{ m}^2\cdot\text{s}^{-1}$), ranges from 1.01×10^5 to 2.58×10^5 . When the Reynolds number is greater than 10^5 , the fluid motion state no longer changes with an increase in the Reynolds number, i.e., dynamic similarity is satisfied (Zhang et al. 2021).

3 Results and Analysis

3.1 Numerical simulation

3.1.1 Streamline characteristics of the wind and sand flow

Fig. 5 is the streamline characteristic diagram of the wind-sand flow with different inlet wind speeds flowing through the 30% porosity HDPE board sand barrier (hereinafter referred to as the sand barrier). When the wind-sand flow passes through the sand barrier, the fluid particles of the wind-sand flow are blocked by the sand barrier around the sand barrier and gradually decelerate. Kinetic energy is continuously consumed. When the wind-sand flow passes through the separation point (the red point in the figure), the kinetic energy of the fluid particles is exhausted, and the fluid particles cannot continue to move forward with the original airflow. After the separation point, the following fluid particles are also hindered by obstacles, and the airflow is forced to stagnate or reverse its movement due to the air

pressure difference. On the leeward side of the sand barrier, the reverse motion of the fluid particles develops rapidly, while the original airflow outside this area continues to move forward, and the two move in opposite directions, resulting in a clockwise vortex with a high vorticity. The vortex continuously consumes the kinetic energy of the wind-sand flow. At the end of the vortex motion, the wind-sand flow particle begins to restore the original airflow motion state. This position is the reattachment point (yellow point in the figure). The magnitude of the vorticity is determined by two inflection points, the separation point and the reattachment point. The magnitude of the vorticity is determined by two inflection points, the separation point and the reattachment point. The vortex motion interacts with the surface friction in the near-surface area, and the motion intensity and the friction force determine the motion state of sand particles on the surface. Therefore, the vortex vorticity represents the sand-blocking performance of the sand barrier.

By analyzing the streamline characteristics of the

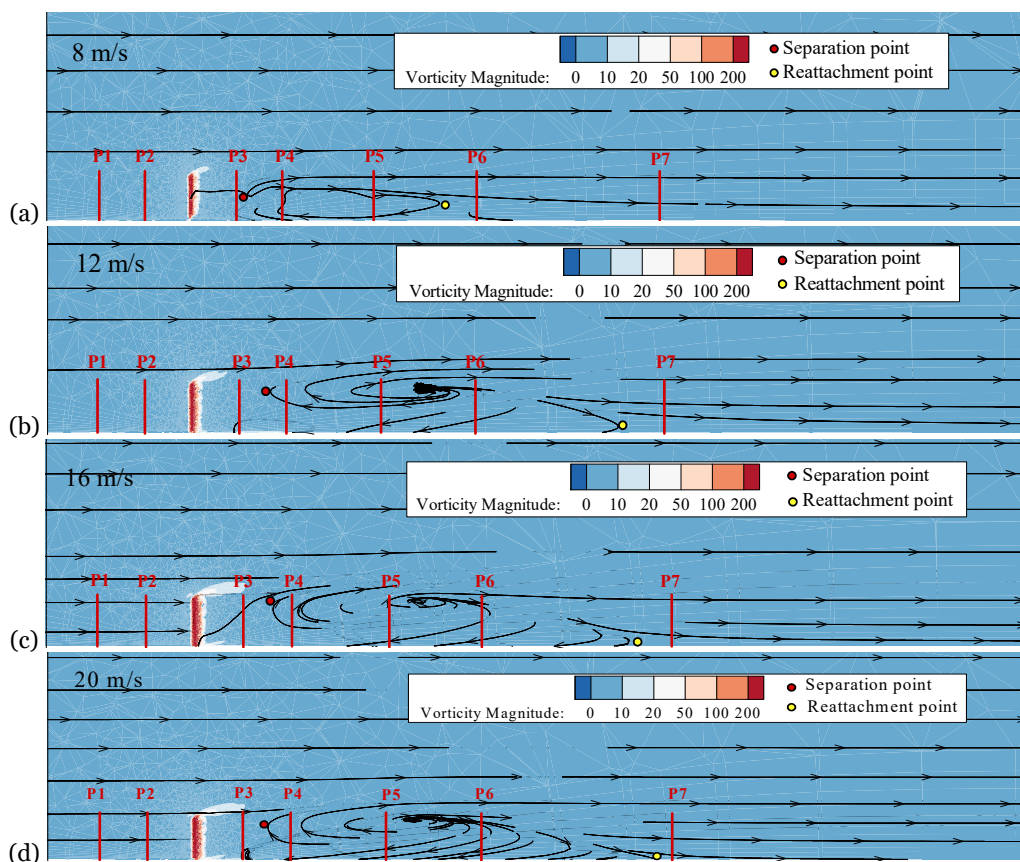


Fig. 5 (a)~(d) Streamline characteristic diagrams around the sand barrier when the inlet wind speeds are 8, 12, 16, and 20 m/s, respectively. The specific positions are 0.5H (P1) on the windward side of the sand barrier, 0.25H (P2), 0.75H (P3), 2.5H (P4), 5H (P5), 7.5H (P6), 12.5H (P7) on the leeward side of the sand barrier.

different inlet wind speeds in Fig. 5, it can be concluded that the size and position of the vortex are related to the inlet wind speed. As the wind speed increases, the positions of the separation point and reattachment point move toward the leeward side, and the distance between them gradually increases.

3.1.2 Wind-speed profiles when different inlet wind speeds flow through the sand barrier

At the position of 0.5H (P1) on the windward side of the sand barrier, 0.25H(P2), 0.75H(P3), 2.5H(P4), 5H(P5), 7.5H(P6), 12.5H(P7) on the leeward side (the positions are shown in Fig. 5), a total of 7 points are selected for dimensionless speed comparison (V_i represents V_x for speed in the X direction and V_z for the speed in the Z direction, respectively. V_H is the velocity in the X-direction at height H).

When comparing the wind-speed profiles around the sand barriers with 30%, 40%, and 50% porosities, it is found that the wind-speed profiles changed regularly. For simplicity, an example analysis of the wind-speed profiles around the 30% porosity sand barrier is shown in Fig. 6. $V_{x1}, V_{x2}, V_{x3}, V_{x4}, V_{z1}, V_{z2}, V_{z3}, V_{z4}$ are the wind-speed profiles in the X direction and the wind-speed profile in the Z direction when the inlet wind speeds are 8, 12, 16, and 20 m/s, respectively. At P1, the wind-sand flow accelerates on the windward side of the fence. As the flow area at the sand barrier decreases, a part of the fluid pass over the sand barrier, and this part of the fluid has to pass at a faster speed to ensure the same flow capacity as the other fluids. Therefore, a vertical wind-speed acceleration zone appears, resulting in an increase in the speed of V_z/V_H at this position. Obstructed by the sand barrier, a portion of the sand grains in the wind-sand flow is deposited here. The positions of P2 and P3 are close to the sand barrier, and V_x/V_H shows a segmental logarithmic growth trend. It is mainly divided into two stages: the first stage is caused by the wind-sand flow flowing through the pores of the sand barrier within the height range of 0-1H, and the second stage is caused by the wind-sand flow that crosses the sand barrier 1H above the ground. At P3, the inlet wind speeds of 8 and 12 m/s have small negative values, indicating that a vortex is generated at a position of 0.75H on the leeward side of the sand barrier. Therefore, the vortex separation

point is located within 0-0.75H on the leeward side of the sand barrier. Owing to the leeward side vortex, reverse erosion and sand sedimentation occur on the ground, which is related to the vortex volume. The positions of P4 and P5 are in the core area of the vortex, and their V_x/V_H values are obviously negative, which reflects the clockwise movement of the wind-sand flow in the vortex movement from another angle. At both locations, significant negative values appear at the inlet wind speeds of 12, 16, and 20 m/s, indicating that the vortex volume at this location is very large, and reverse erosion is likely to occur. At position P4, when compared with positions P2 and P3, V_x/V_H has the second smallest negative value, and the value is the smallest when the inlet wind speed is 16 m/s. This indicates that the location of the separation point on the leeward side of the sand barrier is different at different wind speeds, that is, the location where the vortex appears is also different. At P5, the V_x/V_H of the four inlet wind speeds reach the minimum value; that is, this position is closest to their vortex center among the seven positions. At P6 position, V_x/V_H with an inlet wind speed of 8 m/s is positive, indicating that its vortex has disappeared. The V_x/V_H value of the remaining wind speeds gradually increase and the reattachment point becomes closer. The value at the P7 position returns to the motion state present at the P1 position, and there is no change with increasing height. This position exceeds the influence range of the vortex, and the wind-sand flow restores the motion state of the original airflow.

3.1.3 Wind-speed profiles around the sand barriers with different porosities

As mentioned above, the wind-speed profile around the sand barrier changes regularly under the same porosity. For simplicity, the inlet wind speed of 12 m/s is used as an example for analysis in Fig. 7. $V_{x(30\%)}, V_{x(40\%)}, V_{x(50\%)}, V_{z(30\%)}, V_{z(40\%)}, V_{z(50\%)}$ are the wind-speed profiles in the X direction and the wind-speed profile in the Z direction after passing through the sand barrier with 30%, 40%, and 50% porosity, respectively. At the position of P1, the V_z/V_H characteristic curve has a vertical upward acceleration region, and the larger $\partial V_z/\partial Z$ is, the greater the intensity of the acceleration region is. In the range of 0-1H height, the $\partial V_z/\partial Z$ is the largest when the porosity is 30%, that is, its acceleration zone strength

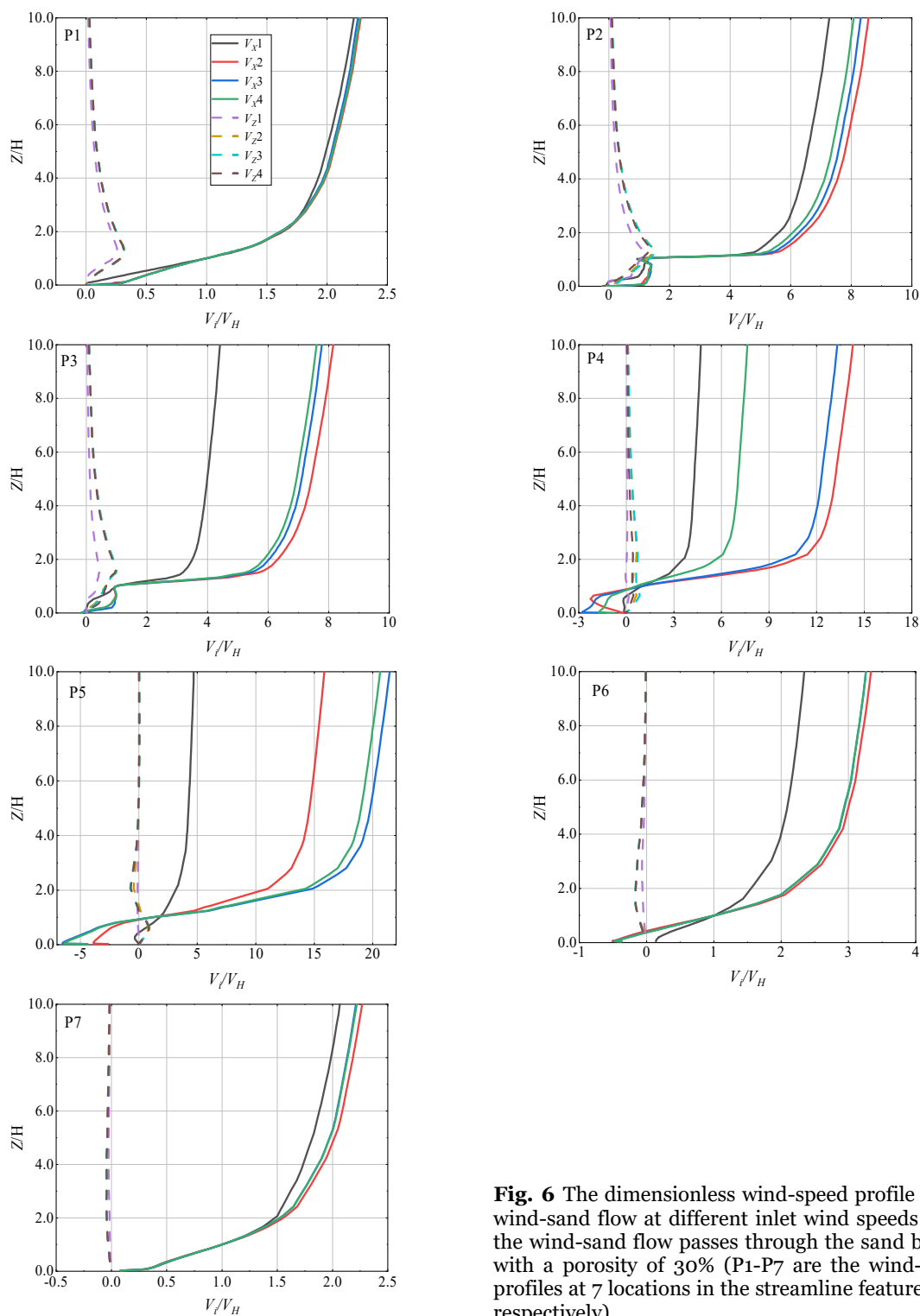


Fig. 6 The dimensionless wind-speed profile of the wind-sand flow at different inlet wind speeds when the wind-sand flow passes through the sand barrier with a porosity of 30% (P1-P7 are the wind-speed profiles at 7 locations in the streamline feature map, respectively).

is the largest. By comparison, it is found that the strength of the acceleration zone is inversely proportional to the porosity. The part of the wind-sand flow passing through the pores of the sand barrier decreases with the decrease of the porosity,

which means that more wind-sand flow needs to pass above the sand barrier. The V_z/V_H characteristic curves at the positions of P2 and P3 are similar to those at the P1 position, while the V_x/V_H characteristic curve shows a piecewise logarithmic

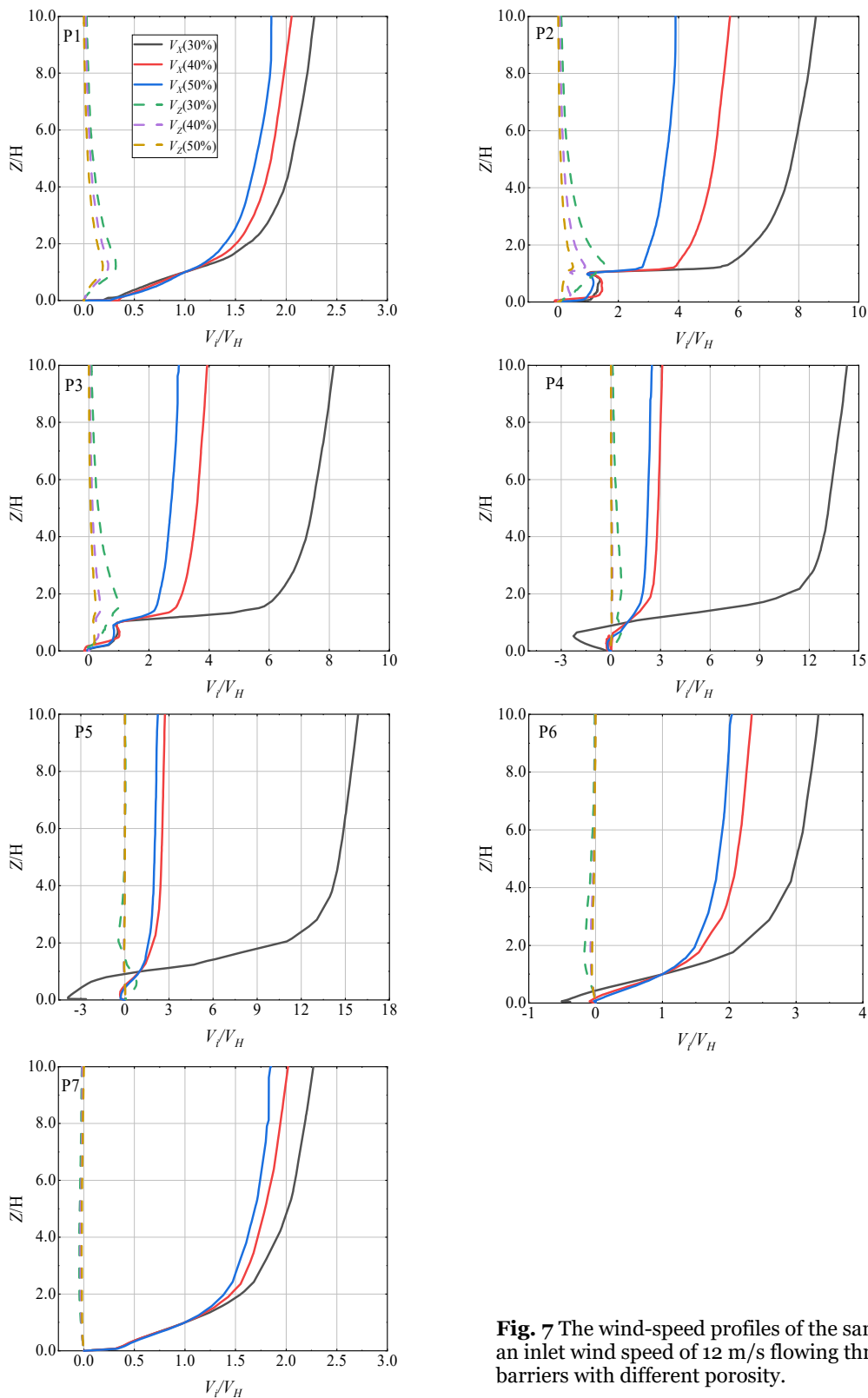


Fig. 7 The wind-speed profiles of the sand flow with an inlet wind speed of 12 m/s flowing through sand barriers with different porosity.

growth trend. At the position of P3, the characteristic curves of V_x/V_H all show negative values, which indicates that the separation points of the three

porosity sand barriers are located in the range of 0-0.75H on the leeward side of the sand barrier. At the P4 position, the negative value of the V_x/V_H

characteristic curve of the 30% porosity sand barrier is further reduced, which is much smaller than other characteristic curves. It shows that the vortex volume on the leeward side of the 30% porosity sand barrier at this location is much larger than that of other porosity, and sedimentation may occur. At the position of P5, in the characteristic curve of the flow field flowing through the sand barrier with 30% porosity, V_x/V_H reaches the minimum value, indicating that this position is closest to the center of its vortex, and therefore reverse erosion may occur. In the wind-speed profile of the 30% porosity sand barrier at the P6 position, the minimum value of the characteristic curve is close to 0, indicating that the P6 position is close to its reattachment point. The characteristic curve of V_x/V_H at the P7 position has returned to the motion state present at the P1 position, and the characteristic curve of V_z/V_H basically does not change with the increase of the height.

3.1.4 Sedimentation and erosion characteristics around the sand barriers

Fig. 8 shows the sedimentation and erosion characteristics of the wind-sand flowing through a sand barrier with 30% porosity. To compare the influence of different inlet wind speeds on sand erosion and sedimentation, 1#, 2#, 3#, and 4# in the figure show the sand sedimentation and erosion characteristic curves at wind speeds of 8, 12, 16, and 20 m/s, respectively. In Fig. 8, the sedimentation mainly occurs on the leeward side of the sand barrier, and on the windward side of the sand barrier, there is only a small amount of sedimentation under the 1# and 2# characteristic curves. Overall, with an increase in wind speed, forward erosion or reverse erosion gradually replaces sedimentation; that is, as the erosion area increases, the sedimentation area gradually shortens. The 1# characteristic curve can be divided into two areas: sedimentation → forward erosion, which begins at the 2H position on the windward side of the sand barrier, and forward erosion, which begins after the sedimentation ends. The distance between the sedimentation areas is as long as 18.9H. With an increase in wind speed, the 2# and 3# characteristic curves can be divided into four different regions: sedimentation → reverse erosion → sedimentation → forward erosion. Among them, the 2# characteristic curve begins to deposit at the position of 0.9H on the windward side of the sand

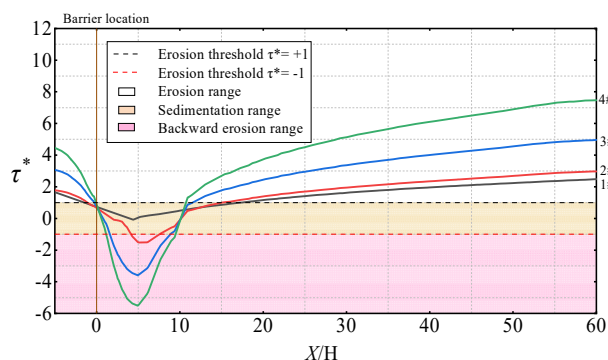


Fig. 8 Sedimentation and erosion characteristics around the sand barrier when the sand flow at different inlet wind speeds passes through the sand barrier with 30% porosity (the white area is forward erosion, the yellow area is sedimentation, the pink area is reverse erosion, 1#, 2 #, 3#, 4# represent the characteristic curves when the inlet wind speed is 8, 12, 16, and 20 m/s, respectively).

barrier, with a distance of 4.8H. Then, reverse erosion occurs at a distance of 3.5H, followed by sedimentation at a distance of 7.7H, and the transition to forward erosion begins after the end of sedimentation. The 3# characteristic curve begins to deposit at the sand barrier with a distance of 1.5H, then reverse erosion at a distance of 6.2H, followed by sedimentation at a distance of 3.7H. Forward erosion begins after the sedimentation. In the 4# characteristic curve, sedimentation begins to appear at the position of the sand barrier at a distance of 1.2H, then reverse erosion occurs at a distance of 8H, followed by sedimentation at a distance of 1.3H. Forward erosion begins to occur after sedimentation. Comparing the reverse erosion distance of the characteristic curves of 2#, 3# and 4#, it can be observed that the greater the wind speed, the longer the reverse erosion distance, reflecting the law that the vorticity is proportional to the wind speed.

To compare the effects of sand barriers with different porosities on sand sedimentation and erosion, Fig. 9 shows the sedimentation and erosion characteristics of the wind-sand flow with an inlet wind speed of 12 m/s flowing through sand barriers with different porosities. 5#, 6#, and 7# in the figure are the characteristic curves of sand sedimentation and erosion after wind-sand flow passes through sand barriers with 30%, 40%, and 50% porosity, respectively. In Fig. 9, the 5# characteristic curve can be divided into four different regions: sedimentation → reverse erosion → sedimentation → forward erosion. Sedimentation begins to appear at 0.9H from

the windward side of the sand barrier, and the distance is $4.8H_1$. Then, reverse erosion occurs at a distance of $3.5H_1$, followed by sedimentation at a distance of $7.7H_1$, and forward erosion begins after sedimentation is over. The characteristic curves of 6# and 7# can be divided into two different regions: sedimentation \rightarrow forward erosion. The 6# characteristic curve begins to deposit at the position of the sand barrier, and the distance is $10.2H_1$; the 7# characteristic curve begins to deposit at the position of the sand barrier, and the distance is $8.5H_1$. The overall trend of the sand barrier characteristic curves of the three porosities is the same, that is the 5# characteristic curve has a part of reverse erosion on the leeward side of the sand barrier.

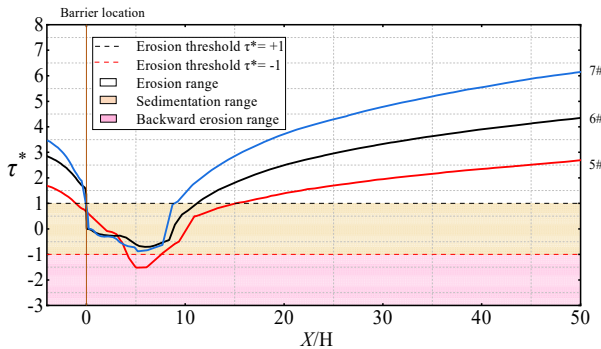


Fig. 9 Sedimentation and erosion characteristics of wind-sand flow around sand barriers with different porosity when the inlet wind speed is 12 m/s (5#, 6# and 7# represent characteristic curves of sand barriers with 30%, 40% and 50% porosity, respectively).

3.2 Wind tunnel test

3.2.1 Wind profile around the sand barrier

Fig. 10(a) shows the wind-speed profile at each measuring point on the windward and leeward sides of the sand barrier with different porosities (30%, 40%, and 50%) at an inlet wind speed of 12 m/s. It can be observed from the figure that at P1, the overall wind-speed profile shows a logarithmic growth trend, and there is almost no difference between the curves. Because the positions of P2, P3, and P4 are close to the sand barrier, it is found that the V_x/V_{H_1} value is the smallest when the porosity is 30% within the height range of $0.2-1H_1$. The second is the V_x/V_{H_1} value with a porosity of 40%, which means that the sand barrier has the best protection effect on the flow field when the porosity is 30%. At positions P5 and

P6, the value of V_x/V_{H_1} at the height of H_1 from the ground is basically unaffected by the sand barrier, and the values of V_x/V_{H_1} with different porosities are basically the same. Within the height range of $0-0.8H_1$ from the ground, the V_x/V_{H_1} value with a porosity of 30% is the smallest, followed by the V_x/V_{H_1} value with a porosity of 40%.

Fig. 10(b) is the wind-speed profile at each measuring point on the windward and leeward sides of the sand barrier with a porosity of 30% under different inlet wind speeds (8, 12, 16 and 20 m/s). It can be seen from the figure that at the P1 position, the overall wind-speed profile shows a logarithmic growth trend, and the change rules of each curve are basically the same. At the P2 position, within the height range of $0.2-0.8H_1$ from the ground, the value of V_x/V_{H_1} is the smallest when the inlet wind speed is 20 m/s, and the value of V_x/V_{H_1} is the largest when the inlet wind speed is 8 m/s. The negative values of V_x/V_{H_1} appear at the positions of P3, P4 and P5. The negative value of V_x/V_{H_1} at the inlet wind speed of 20 m/s is the smallest, and the negative value of V_x/V_{H_1} at the inlet wind speed of 8 m/s is the largest. It shows that the reverse erosion of the leeward side V_x/V_{H_1} of the sand barrier increases with the increase of the inlet wind speed. At the positions of P6 and P7, when the inlet wind speed is 8 m/s, the V_x/V_{H_1} value restores the original inflow wind-speed profile the fastest.

3.2.2 Erosion and sedimentation around the sand barriers

In the wind tunnel test, when the inlet wind speed is 12 m/s, the sedimentation distances around the sand barriers with porosities of 30%, 40%, and 50% are shown in Fig. 11. When the porosity is 30%, the sedimentation distance on the leeward side of the sand barrier is approximately $9H_1$, when the porosity is 40%, the sedimentation distance on the leeward side of the sand barrier is approximately $8H_1$; and when the porosity is 50%, the sedimentation distance on the leeward side of the sand barrier is approximately $6.5H_1$. It can be concluded that the sedimentation distance is negatively correlated with the porosity of the sand barrier. The sedimentation distance on the leeward side of the sand barrier at different inlet wind speeds when the porosity is 30%

is shown in Fig. 12. When the inlet wind speeds are 8, 12, 16, and 20 m/s, the sedimentation distances on the leeward side of the sand barrier are $12H_1$, $9H_1$, $5H_1$, and $3H_1$, respectively; this sedimentation distance is negatively correlated with the inlet wind speed.

4 Discussion

4.1 Wind-speed profile

By comparing the wind tunnel test and numerical simulation results, when the sand barrier porosity is 30%, the negative values of the wind-speed profile in the X direction all appear near the $0.75H_1$ position on the leeward side of the sand barrier and disappear near the $7.5H_1$ position on the leeward side of the sand barrier, indicating that their leeward side vortices appear at similar locations. Taking the inlet wind speed of 12 m/s as an example, the numerical simulation results show that the wind-speed profile in the X direction is within the range of $2.5H_1$ - $7.5H_1$ on the leeward side of the sand barrier. The negative value of wind velocity profile of sand barrier with porosity of 30% is far less than that of wind velocity profile of sand barrier with porosity of other values. The smaller the negative value, the greater the vorticity on the leeward side of the sand barrier and the better the protection effect of the sand barrier. By observing the wind-speed profile in the Z direction, it is found that the smaller the porosity of the sand barrier, the greater the slope of the wind-speed profile, that is, the greater the strength of the acceleration zone. The above

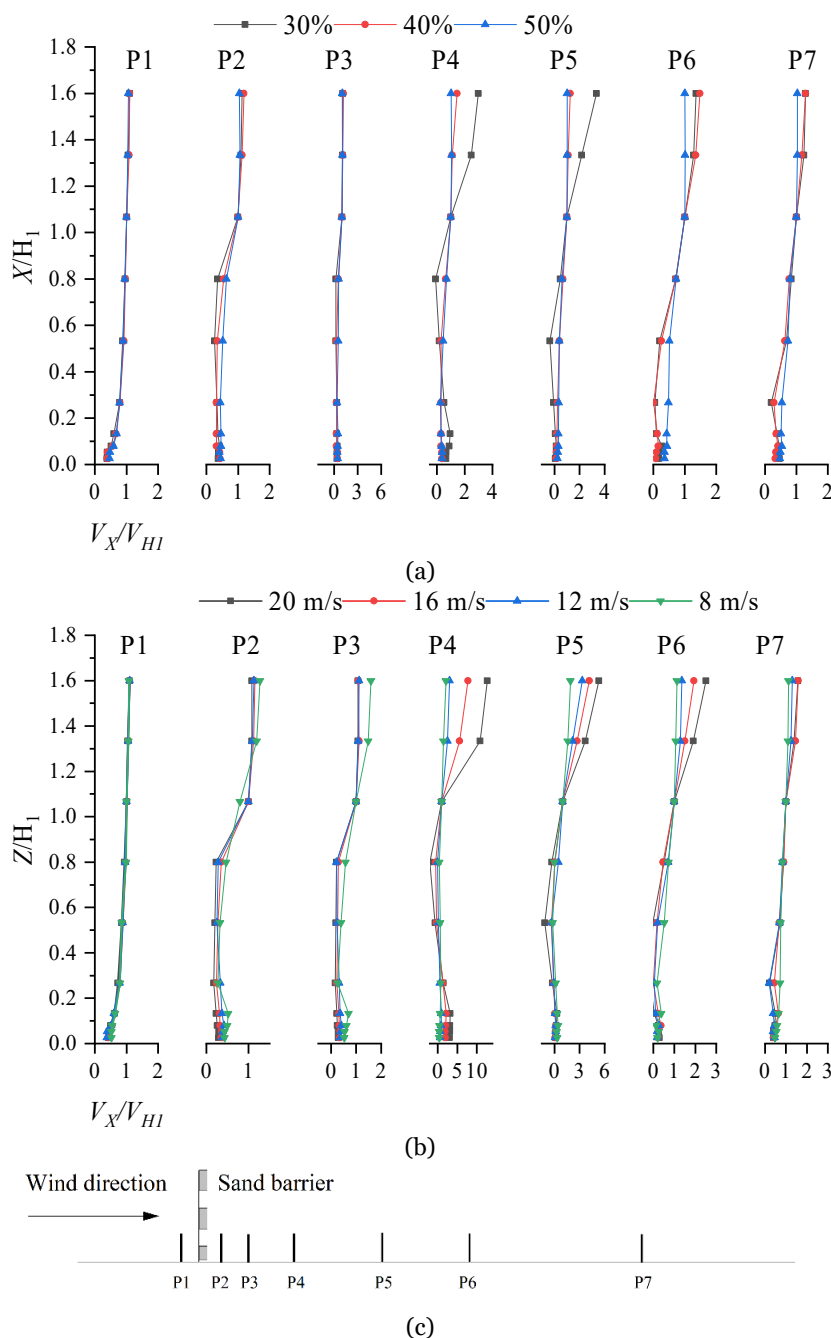


Fig. 10 (a) Wind-speed profiles at each different position on the windward and leeward sides of the sand barrier with different porosities when the inlet wind speed is 12 m/s. (b) Wind-speed profiles at each position on the windward side and the leeward side of the sand barrier with different inlet wind speeds when the porosity is 30%. (c) P1-P7, the positions of the seven points in the numerical simulation are the same under the dimensionless condition.

results show that a sand barrier with a porosity of 30% has a significantly better protective effect on sand flow than those with porosities of 40% and 50%. Zhang et al. (2019) used the same inlet wind speed and analyzed the wind speeds at different heights and the results are

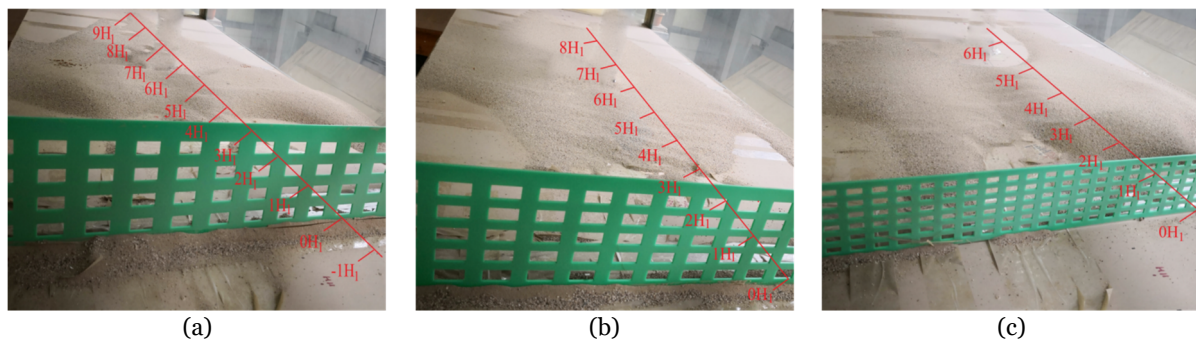


Fig. 11 When the inlet wind speed is 12 m/s, the resulting sand accumulation around the sand barrier is shown (a, b, and c are the HDPE board sand barrier with porosity of 30%, 40% and 50%, respectively).

consistent with the results of this study, that is, a sand barrier with a porosity of 30% has the most obvious protection effect. Tsukahara et al. (2012) used visible laser technology to monitor the flow field and sand dune erosion around dunes and found that a sand barrier with a porosity of 30% had the best protection effect, which was found in this study.

4.2 Erosion and sedimentation

In the numerical simulation, the wind-speed profile around the sand barrier with a porosity of 30% shows that when the wind sand flows through the sand barrier with different inlet wind speeds, the position and size of the vortex created on the leeward side of the sand barrier are different. With an increase in wind speed, the vortex position moves in the direction of the wind-sand flow, and the distance between the separation point and the reattachment point increases; that is, the vorticity is larger. In the wind tunnel test, the measured wind-speed profiles at different inlet wind speeds are consistent with the numerical simulation results; that is, the greater the wind speed, the greater the vorticity on the leeward side of the sand barrier. In the numerical simulation, the sedimentation and erosion distances around the sand barriers with different porosities are shown in Fig. 13. When the inlet wind speed is 8 m/s, the sedimentation distance on the leeward side of the sand barriers is as long as 18.9H. The other three wind speeds show reverse erosion on the leeward side of the sand barrier. With an increase in wind speed, the sedimentation area decreases, and the reverse erosion area increases. The closer the location of the restoration erosion is to the sand barrier, the sedimentation distances are 12.5H, 5.2H and 2.5H when the inlet wind speeds are 12, 16, and 20 m/s, respectively. Fig. 14 shows the sedimentation and

erosion distances around the sand barriers with different porosities. When the inlet wind speed is 12 m/s, the sand barrier with a porosity of 30% exhibits sedimentation and partial reverse erosion on the leeward side, and the sedimentation distance is 12.5H. However, the sand barriers with 40% and 50% porosity are only deposited on the leeward side, and the sedimentation distances are 10.2H and 8.5H, respectively, which are similar to the results in the wind tunnel test. As the distance increases, the point where erosion is restored was further away from the sand barrier. Zhang et al. (2020) studied the distribution of sand accumulation around sand barriers with different porosities and found that when the porosity was 30%, the sand accumulation around the sand barriers was significantly higher than that around sand barriers with other porosities. However, when the porosity was 30%, sand accumulation was mainly distributed on the windward side of the sand barrier, which was inconsistent with the results presented in this paper. The reason for this phenomenon may be that Zhang et al. (2020) used the volume fraction of the sand phase to characterize sand accumulation around the sand barrier. Jin et al. (2005) found in field investigation that with the increase of wind speed, the amount of sand deposited around the fence decreased correspondingly, which was consistent with the study in this paper. Wang et al. (1999) investigated the field site and found that the deposition distance of sand grains around the sand barrier was about 1-7 H, and most of the sand grains deposition distance was 3-5 H. However, the specific wind speed and porosity of the sand barrier were not explained in the paper.

The numerical simulation and the wind tunnel test sedimentation distances are compared with the dimensionless values. In the wind tunnel test, the sedimentation distance is divided by the height of the

sand barrier model (H_1) to obtain the dimensionless sedimentation distance of the wind tunnel test. In the numerical simulation, the sedimentation distance is divided by the height of the sand barrier model (H) to obtain the dimensionless sedimentation distance of the numerical simulation. The dimensionless sedimentation distances are compared. Fig. 15(a) shows a comparison of the sedimentation distance between the numerical simulation and the wind tunnel test under an inlet wind speed of 12 m/s. When the porosity is 30%, the ratio of the length of the sedimentation distance is 1.4. When the porosity is 40%, the ratio of the length of the sedimentation distance is 1.3. When the porosity is 50%, the ratio of the length of the sedimentation distance is 1.3. The average ratio of sedimentation distance between the numerical simulation results and the wind tunnel test results is 1.3. The reason for the error may be the slight difference between the wind-speed profile of the numerical simulation and the wind tunnel test. Fig. 15(b) shows a comparison between the sedimentation results of the numerical simulation and the wind tunnel test when the porosity is 30%. The two sedimentation distances are consistent: the greater the wind speed, the shorter the sedimentation distance on the leeward side of the sand barrier. When the wind speed is 8 m/s, the ratio of the sedimentation distance length between the numerical simulation and wind tunnel test is 1.6; when the wind speed is 12 m/s, the ratio of the two is 1.4; when the wind speed is 16 m/s,

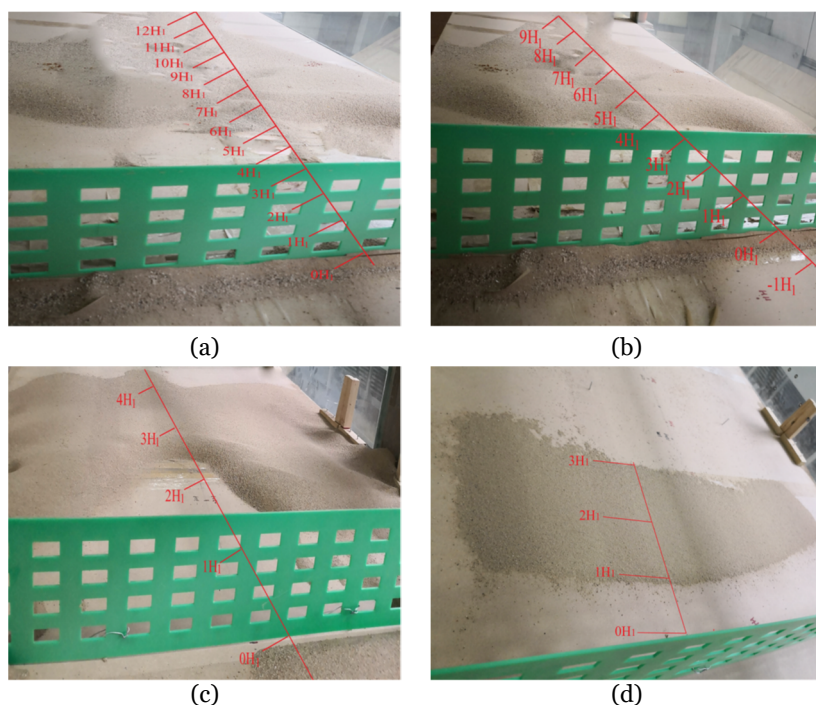


Fig. 12 When the porosity of the HDPE board sand barrier is 30%, the resulting sand sedimentation around the sand barrier is shown (a, b, c, d shows the sand sedimentation when the inlet wind speeds are 8, 12, 16 and 20 m/s, respectively).

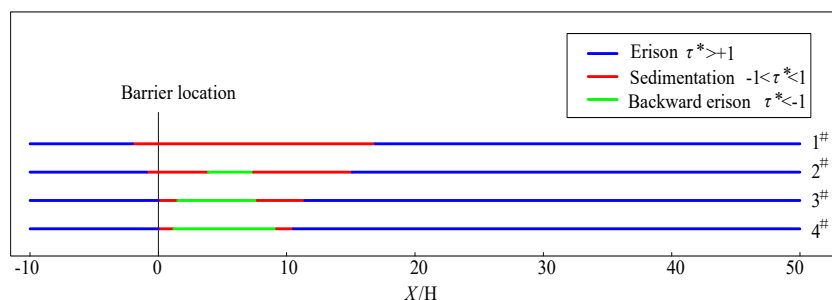


Fig. 13 The sedimentation and erosion distances around the sand barrier when the porosity is 30% under different incoming wind speeds (1#, 2#, 3#, and 4# represent the length of sedimentation and erosion around the 30% porosity sand barrier when the wind speed is 8, 12, 16, and 20 m/s, respectively).

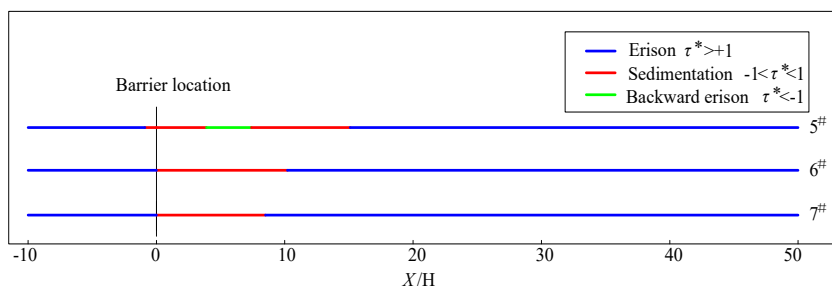


Fig. 14 Sedimentation and erosion distances around sand barriers with different porosity when the incoming wind speed is 12 m/s (5#, 6#, 7# are the surrounding sedimentation and erosion lengths when the wind speed is 12 m/s and the porosity is 30%, 40%, and 50%, respectively).

the ratio of the two is 1.0; when it is 20 m/s, the ratio of the two is 0.8. The average ratio of the sedimentation distance of the numerical simulation results to that of the wind tunnel test results is 1.2, and the numerical simulation results are in good agreement with the wind tunnel test results.

5 Conclusions

This paper presents a streamline feature map around a sand barrier and the wind-speed profiles corresponding to multiple feature points, showing the characteristics of the wind-sand flow field around the sand barrier. The possible sedimentation distance and sand erosion on the surface near the sand barrier are described by the ratio of the local shear stress on the ground to the critical shear stress of the sand grains. In particular, sand erosion and sedimentation area maps of three porosity sand barriers under different inlet wind speeds are drawn, which can be understand the sand sedimentation and erosion distances around sand barriers with different porosities. The numerical simulation results are verified by analyzing the data measured by the wind tunnel test. The main conclusions of this study are as follows:

(1) On the leeward side of the sand barrier, the reverse motion of the fluid particles developed rapidly, while the original airflow outside this area continued to move forward, and the two moved in opposite directions, resulting in a high-vorticity vortex moving in a clockwise direction. When the porosity was the same, the size and position of the

vortex on the leeward side of the sand barrier were related to the inlet wind speed. As the wind speed increased, the vortex volume increased, and the positions of the separation point and reattachment point moved toward the leeward side. Under the same inlet wind speed, when the porosity of the sand barrier was 30%, the intensity of the acceleration zone situated above the barrier was the largest. The comparison shows that the strength of the acceleration zone was negatively correlated with porosity.

(2) The erosion sedimentation distance was related to wind speed. When the porosity of the sand barrier was 30%, with the increase in wind speed, the forward erosion or reverse erosion area on the leeward side of the sand barrier gradually replaced the sedimentation area. This meant that the erosion area gradually increased and the sedimentation area gradually shortened. With an increase in porosity, the sedimentation distance on the leeward side of the sand barrier gradually shortened, the erosion area gradually disappeared, and the sedimentation distance on the leeward side of the sand barrier with 30% porosity was the longest.

(3) A comparison between the sedimentation results of the wind tunnel test and the numerical simulation showed that the greater the wind speed, the shorter the sedimentation distance on the leeward side of the sand barrier, and the two sedimentation distances were consistent. Combined with the results of the numerical simulation and wind tunnel test, when the porosity was 30%, the protection effect of the HDPE board sand barrier was better.

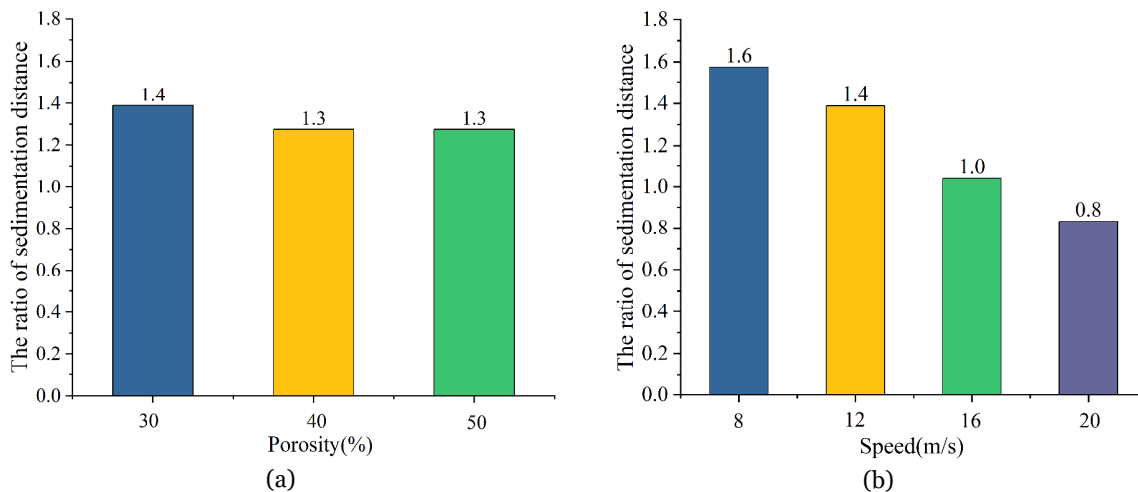


Fig. 15 The ratio of sedimentation distances around sand barriers between numerical simulation and wind tunnel test. (a) The ratio of sedimentation distances around sand barriers at an inlet wind speed of 12 m/s. (b) The ratio of sedimentation distances around the sand barrier when the porosity is 30%.

Acknowledgments

This research was financially supported by the fellowship of the China Postdoctoral Science Foundation (2021M703466), the Natural Science Foundation of Gansu Province, China (20JR10RA231), the Basic Research Innovation

Group Project of Gansu Province, China (21JR7RA347), an Special Funds for Guiding Local Scientific and Technological Development by the Central Government (22ZY1QA005).

References

- Bruno L, Fransos D (2015) Sand transverse dune aerodynamic: 3d coherent flow structures from a computational study. *J Wind Eng Ind Aerod* 147: 291-301.
<https://doi.org/10.1016/j.jweia.2015.07.014>
- Bruno L, Horvat M, Raffaele L (2018) Windblown sand along railway infrastructures: a review of challenges and mitigation measures. *J Wind Eng Ind Aerod* 177: 340-365.
<https://doi.org/10.1016/j.jweia.2018.04.021>
- Dong ZB, Luo WY, Qian GQ (2007) A wind tunnel simulation of the mean velocity fields behind upright porous fences. *Agr Forest Meteorol* 146(1-2): 82-93.
<https://doi.org/10.1016/j.agrformet.2007.05.009>
- Horvat M, Bruno L, Khri S (2021) CWE study of wind flow around railways: Effects of embankment and track system on sand sedimentation. *J Wind Eng Ind Aerodyn* 208: 104476.
<https://doi.org/10.1016/j.jweia.2020.10.4476>
- Jin CN, Dong ZD, Li JJ, et al. (2005) Blown sand deposits and its indications on wind activities around high windbreaks. *J of Des Res* 25(5): 652-657. (In Chinese)
- Lauder BE, Spalding DB (1974) The numerical computation of turbulent flows. *Comput Method Appl M* 3(2): 269-289.
[https://doi.org/10.1016/0045-7825\(74\)90029-2](https://doi.org/10.1016/0045-7825(74)90029-2)
- Lee SJ, Kim HB (1999) Laboratory measurements of velocity and turbulence field behind porous fences. *J Wind Eng Ind Aerod* 80(3): 311-326.
[https://doi.org/10.1016/S0167-6105\(98\)00193-7](https://doi.org/10.1016/S0167-6105(98)00193-7)
- Li BL, Sherman DH (2015) Aerodynamics and morphodynamics of sand fences: A review. *Aeolian Res* 17: 33-48.
<https://doi.org/10.1016/j.aeolia.2014.11.005>
- Li KC, Zhou Q, Ding IS, et al. (2019) Prevention mechanism and effect evaluation of HDPE sand barrier in gobi area of southern Xinjiang. *China Rail Sci* 40(3): 10-14. (In Chinese)
- Lima IA, Parteli EJR, Shao YP, et al. (2020) CFD simulation of the wind field over a terrain with sand fences: Critical spacing for the wind shear velocity. *Aeolian Res* 43: 100574.
<https://doi.org/10.1016/j.aeolia.2020.100574>
- Liu BL, Qu JJ, Zhang WM, et al. (2011) Numerical simulation of wind flow over transverse and pyramid dunes. *J Wind Eng Ind Aerod* 99: 879-888.
<https://doi.org/10.1016/j.jweia.2011.06.007>
- Menter FR, Kuntz M, Langtry R (2003) Ten years of industrial experience with the SST turbulence model. In: Hanjalic K, Nagano Y, Tummers J (Eds.), *Turbulence Heat and Mass Transfer 4: Proceedings of the Fourth International Symposium on Turbulence, Heat and Mass Transfer*, Antalya, Turkey, 12-17 October, 2003. Begell House, p. 1208.
- Noguchi Y, Suzuki M, Baker C, et al. (2019) Numerical and experimental study on the aerodynamic force coefficients of railway vehicles on an embankment in crosswind. *J Wind Eng Ind Aerod* 184: 90-105.
<https://doi.org/10.1016/j.jweia.2018.11.019>
- Perera MDAES (1981) Shelter behind two-dimensional solid and porous fences. *J Wind Eng Ind Aerod* 8(1-2): 93-104.
[https://doi.org/10.1016/0167-6105\(81\)90010-6](https://doi.org/10.1016/0167-6105(81)90010-6)
- Qu JJ, Yu WB, Qin XB, (2014) Wind-protecting efficiency of HDPE functional sand-fixing barriers. *J Des Res* 34(5): 1185-1193. (In Chinese)
- Raffaele L, Bruno L, Pellerey F, et al. (2016) Windblown sand saltation: a statistical approach to fluid threshold shear velocity. *Aeolian Res* 23: 79-91.
<https://doi.org/10.1016/j.aeolia.2016.10.002>
- Smyth TAG (2016) A review of computational fluid dynamics (CFD) airflow modelling over aeolian landforms. *Aeolian Res* 22: 153-164.
<https://doi.org/10.1016/j.aeolia.2016.07.003>
- Tan LH, Zhang WM, Bian K (2016) Numerical simulation of three-dimensional wind flow patterns over a star dune. *J Wind Eng Ind Aerod* 159: 1-8.
<https://doi.org/10.1016/j.jweia.2016.10.005>
- Tominaga Y, Okaze T, Mochida A (2018) Wind tunnel experiment and CFD analysis of sand erosion/deposition due to wind around an obstacle. *J Wind Eng Ind Aerod* 182: 262-271.
<https://doi.org/10.1016/j.jweia.2018.09.008>
- Tsukahara T, Sakamoto Y, Aoshima, D, et al. (2012) Visualization and laser measurements on the flow field and sand movement on sand dunes with porous fences. *Exp Fluids* 52(4): 877-890.
<https://doi.org/10.1007/s00348-011-1157-4>
- Wang T, Qu JJ, Ling YQ, et al. (2017) Wind tunnel test on the effect of metal net fences on sand flux in a Gobi Desert, China. *J Arid Land* 9(6): 888-899.
<https://doi.org/10.1007/s40333-017-0068-5>
- Wang T, Qu JJ, Ling YQ, et al. (2018) Shelter effect efficacy of sand fences: A comparison of systems in a wind tunnel. *Aeolian Res* 30: 32-34.
<https://doi.org/10.1016/j.aeolia.2017.11.004>
- Wang XM, Chen GT, Han ZW, et al. (1999) The benefit of the prevention system along the desert highway in Tarim Basin. *J Des Res* 19(2): 120-127. (In Chinese)
- White BR (1996) Laboratory simulation of aeolian sand transport and physical modeling of flow around dunes. *Ann Arid Zone* 35: 187-213.
<https://doi.org/10.1007/s00585-996-0986-6>
- Wu XX, Zou XY, Zhang CL, et al. (2013) The effect of wind barriers on airflow in a wind tunnel. *J Arid Environ* 97: 73-83.
<https://doi.org/10.1016/j.jaridenv.2013.05.003>
- Yang Y, Gu M, Chen SQ, et al. (2009) New inflow boundary conditions for modelling the neutral equilibrium atmospheric boundary layer in computational wind engineering. *J Wind Eng Ind Aerod* 97(2): 88-95.
<https://doi.org/10.1016/j.jweia.2008.12.001>
- Zakeri JA, Esmaili M, Mosayebi S, et al. (2012) Effects of vibration in desert area caused by moving trains. *J Mod Transp* 20: 16-23.
<https://doi.org/10.1007/BF03325772>
- Zhang K, Wang QC, Yang ZJ, et al. (2019) Research on numerical simulation on wind protection benefits of HDPE panels with high vertical sand barrier in the newly-built Golmud-korla railway. *J China Railw Soc* 41(3): 169-175. (In Chinese)
- Zhang K, Zhao PW, Zhang XX, et al. (2020) Study on difference of wind-sand flow of HDPE board high vertical sand fence by wind velocity profile. *J China Railw Soc* 42(9): 143-149. (In Chinese)
- Zhang K, Zhao PW, Zhao JC, et al. (2021) Protective effect of multi-row HDPE board sand fences: A wind tunnel study. *Int Soil Water Conse* 9: 103-115.
<https://doi.org/10.1016/j.iswcr.2020.08.006>
- Zhang K, Zhao LM, Zhang HL, et al. (2022) Numerical simulation on flow field, wind erosion and sand sedimentation patterns over railway subgrades. *J Mt Sci* 19: 2968-2986.
<https://doi.org/10.1007/s11629-022-7396-4>
- Zhang J, Wang J, Tan X, et al. (2019) Detached eddy simulation of flow characteristics around railway embankments and the layout of anemometers. *J Wind Eng Ind Aerod* 193: 103968.
<https://doi.org/10.1016/j.jweia.2019.10.3968>